Available online at www.sciencedirect.com
ScienceDirect
International Journal of Heat and Mass Transfer 50 (2007) 2624–2633
International Journal of HEAT and MASS TRANSFER
www.elsevier.com/locate/ijhmt

Perturbation solution for solidification of pure metals on a sinusoidal mold surface

Faruk Yigit

Department of Mechanical Engineering, King Saud University, P.O. Box 800, Riyadh 11421, Saudi Arabia

Received 11 April 2006; received in revised form 27 September 2006
Available online 17 January 2007

Abstract

A linear perturbation method is used to solve two-dimensional heat conduction problem in which a liquid, becomes solidified by heat transfer to a sinusoidal mold of finite thickness. The finite difference method is used to discretize the governing equations. The molten metal perfectly wets the mold surface prior to the beginning of solidification, and this leads to a corresponding undulation of the metal shell thickness. The influence of physical parameters such as the thermal capacities of shell and mold materials, and mold surface wavelength on the growth of solidified shell thickness is investigated. Analytical results are obtained for the limiting case in which diffusivities of the solidified shell and the mold materials are infinitely large, and compared with the numerical predictions to establish the validity of the model and the numerical approach.

Keywords: Solidification; Growth instability

1. Introduction

Phase-change problems involving melting or solidification are of considerable practical importance, because of applications to the process of casting, welding and the formation of ice [1]. In addition, preparation of semiconductor-grade silicon crystals which can only be produced by growth from the melt is an essential step in modern solid-state physics [2]. Exact treatment of such problems is very difficult because the location of the moving interface is not known a priori and must follow as a part of the solution. Due to the non-linear nature of governing equations, only a limited number of analytical solutions to such problems have been proposed. A review of literature on the subject can be found in Refs. [3,4].

During the casting process, an initially liquid mass of material is caused to solidify by reducing its temperature below the melting point by heat transfer from its surfaces, which are in contact with a surrounding mold. The process therefore generally starts by the formation of a solidified shell in contact with the mold and surrounding the remaining liquid mass. If solidification is interrupted, periodic thickness non-uniformities at the freezing front are often observed that can have wavelengths of the order of several centimeters. If solidification is allowed to proceed, however, the non-uniformities tend to die out as the freezing front morphology becomes less dependent upon the mold–shell interface due to the ever-thickening shell. Such microstructures are detrimental to subsequent forming processes and have linked to severe ingot cracking [5]. Experimental observations of thermo-mechanical growth instability in casting processes have been reported by Cisse et al. [6], Singh and Blazek [7], and Wray [8]. Theoretical models of the proposed growth instability mechanism during solidification of pure metals have been presented by Richmond et al. [9], Yigit et al. [10], Yigit and Barber [11], and Yigit and Hector [12,13]. It has been suggested that patterned mold surface geometries may help to promote the uniform growth of a casting and hence deter the onset of the

E-mail address: fyigit@ksu.edu.sa

0017-9310/$ - see front matter © 2006 Elsevier Ltd. All rights reserved.
doi:10.1016/j.ijheatmasstransfer.2006.11.023

Nomenclature

a_1, a_2	amplitude of the upper and lower sinusoidal mold surfaces [m]
h_0	nominal mold thickness [m]
k	diffusivity [$m^2\ s^{-1}$]
K	conductivity [$W\ m^{-1}\ °C^{-1}$]
l	$\lambda/2\pi$ [m]
L	latent heat of fusion [$J\ kg^{-1}$]
m	$1/l$ [m^{-1}]
R_0	thermal contact resistance [$m^2\ s\ °C\ J^{-1}$]
t	time [s]
T	temperature [°C]
T_m	melting temperature [°C]
s	solidified shell thickness [m]
Q	heat flux [$J\ m^{-2}\ s^{-1}$]
x, y	Cartesian coordinates [m]

Subscripts

0,1	zeroth and first-order, respectively

Superscripts

c, d	shell and mold materials, respectively

Greek symbols

δ	space step size
ϵ_1, ϵ_2	upper and lower mold surface aspect ratios, respectively
λ	wavelength [m]
ρ	density [$kg\ m^{-3}$]
τ	time increment

observed shell thickness non-uniformities [14–16]. Murakami et al. [15] proposed that periodic grooves in the mold surface, which led to gaps of a controlled size along the mold–shell interface due to imperfect wetting of the molten metal, resulted in a number of important improvements. Perhaps, the most significant improvements were more uniform contact along the mold–shell interface, and a reduction in crack nucleation in the ingot due to slower, but more uniform heat extraction. To test this hypothesis, the immersion tests were repeated for aluminum alloys using casting molds with machined grooves [16]. A key parameter that was investigated was the groove pitch or wavelength and their impact on the shell thickness non-uniformity. It was suggested that there was a possibility of a wavelength selection process wherein the system "picked-off" a mold surface wavelength or band of wavelengths such that the shell grew with greater uniformity. For a smooth mold surface (or at least one with no prominent periodicity), the perturbations in heat extraction result from stochastic variations in the mold–shell interface heat flux due to a variety of process-related conditions and material properties/metallurgical transformations. An equally random display of thickness irregularities in the shell results during the early stages of solidification: as the shell thickens, the mold–shell boundary conditions have a diminishing impact on the growth of irregularities at the freezing front. In the idealized case of a mold surface with a purely sinusoidal topography (for example), the controlling factor is the topography geometry, since this creates a spatial perturbation in the heat extraction profile.

It is the purpose of the present paper to investigate the combined effects of thermal capacities of the solidified shell and mold materials, and mold surface wavelength on the growth of solidified shell thickness in a one-dimensional solidification process which occurs on a sinusoidal mold of low aspect ratio (i.e., the ratio of the amplitude to wavelength is much less than one). Thus, the present paper can be considered as a first step toward achieving a complete thermo-mechanical model to understand the aforementioned shell thickness non-uniformities. The present heat conduction model can be combined to a thermoelastic deformation model to examine the development of the residual thermal stresses and the contact pressure at the mold–shell interface for the analysis of thermoelastic contact since the perturbation method described here provides stability criterion for the physics of growing solid and its deformation. In this paper, we shall obtain solution for the advance of the solid/melt boundary. In particular, we investigate the interactions of non-zero thermal capacities of the shell and mold materials against each other and mold surface wavelengths which were not studied in previous models cited above. The solution is developed by a linear perturbation method which leads to the unidirectional unperturbed process to be uncoupled from the first-order perturbed solution, and permits the two problems to be solved sequentially.

2. Formulation of the problem

We consider a single-phase solidification problem where the temperature in the liquid region is assumed to be spatially uniform and constant in time, equal to the melting temperature T_m. Solidification takes place at a distinct temperature, and the solid and liquid phases are separated by a sharp moving interface since the present analysis is restricted by the solidification of pure materials. Initially, there is a very thin solidified layer which is compliant to a sinusoidal mold of mean thickness h_0. Both the upper surface of the mold, which is in contact with the shell along $y = 0$, and the lower surface at $y = -h_0$, have sinusoidal surface topographies of wavelength λ. The heat flux drawn from the bottom of the mold is prescribed as a constant. After a time t, the liquid solidified near the mold forms a solid shell thickness $s(x,t)$. Thus, $s(x,t)$ defines the moving

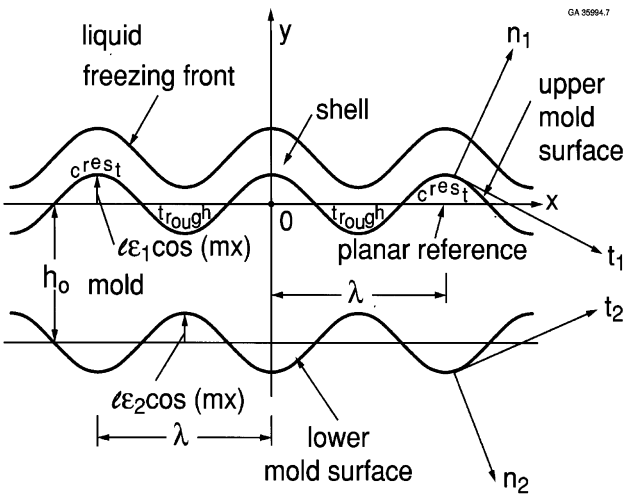

Fig. 1. Geometry of the system.

interface between the solid and liquid phases as shown in Fig. 1. We assume that densities ρ^c, ρ^d, thermal diffusivities k^c, k^d, and conductivities K^c, K^d of the solid phase and the mold are constant and independent of temperature and time. The temperature of the solidified shell and the mold $T^c(x,y,t)$, $T^d(x,y,t)$ must satisfy the heat conduction equations:

$$\nabla^2 T^c = \frac{1}{k^c}\frac{\partial T^c}{\partial t}; \quad \nabla^2 T^d = \frac{1}{k^d}\frac{\partial T^d}{\partial t}, \quad t > 0 \tag{1}$$

which are subject to the following initial and boundary conditions:

$$s(x,0) = l\epsilon_1 \cos(mx) \tag{2}$$

$$T^c(x,s,t) = T_m \tag{3}$$

$$K^c \frac{\partial T^c}{\partial y}(x,s,t) = L^c \rho^c \frac{\partial s}{\partial t}(x,t) \tag{4}$$

$$K^c \frac{\partial T^c}{\partial y}(x,y_1,t) = K^d \frac{\partial T^d}{\partial y}(x,y_1,t); \quad y_1 = l\epsilon_1 \cos(mx) \tag{5}$$

$$K^c \frac{\partial T^c}{\partial y}(x,y_1,t) = \frac{1}{R_0}\left[T^c(x,y_1,t) - T^d(x,y_1,t)\right] \tag{6}$$

$$K^d \frac{\partial T^d}{\partial y}(x,y_2,t) = Q; \quad y_2 = -(h_0 + l\epsilon_2 \cos(mx)) \tag{7}$$

where L^c is the latent heat of fusion of the solidified material and R is the thermal contact resistance at the mold/solid interface. We define

$$\epsilon_1 = a_1/l; \quad \epsilon_2 = a_2/l \tag{8}$$

as the upper and the lower mold surface aspect ratios, respectively, where $l = \lambda/2\pi = 1/m$ and a_1, a_2 are, respectively, the amplitudes of the upper and lower sinusoidal mold surfaces.

Eq. (2) implies that there is a very thin solidified shell which is compliant to the sinusoidal mold surface at initial time. Eq. (3) states that freezing front is isothermal at the melting temperature, while (4) defines an energy balance between the heat conducted away from the moving interface into the solidified shell and the latent heat released during solidification. Eq. (5) states that heat flux from the casting to the mold must be continuous. There will generally be some thermal contact resistance R_0 at the mold–shell interface due to the effects of surface roughness and surface or contaminants films. Temperature difference due to the imperfect contact at this interface is described by the boundary condition (6), and heat flux is prescribed at the bottom of the mold as given in Eq. (7).

3. The perturbation method

The modest spatial variation in the upper mold surface leads to a corresponding spatial perturbation of the temperature fields in the shell, the mold, and the freezing front once solidification begins, i.e.

$$T^i(x,y,t) = T_0^i(y,t) + T_1^i(y,t)\cos(mx) \tag{9}$$
$$T_1^i(y,t) \ll T_0^i(y,t); \quad (i = c,d)$$

$$s(x,t) = s_0(t) + s_1(t)\cos(mx) \tag{10}$$
$$s_1(t) \ll s_0(t)$$

Notice that suffix 0 refers to the x-independent zeroth-order process, and the problem has a simple one-dimensional solution which is called the "zeroth-order" solution. However, suffix 1 refers to the amplitude of the sinusoidal perturbation or first-order process. It is assumed that the amplitude of this perturbation is small in comparison with its wavelength (i.e., $ms_1(t) \ll 1$), in which case the slope of the moving front, $\partial s/\partial x$, is very much less than unity. It then follows that the heat flux in the x-direction is negligible to the first-order.

Substituting Eq. (9) into the Eq. (1) and separating periodic and uniform terms in x, we obtain

$$\frac{\partial^2 T_0^c}{\partial y^2}(y,t) = \frac{1}{k^c}\frac{\partial T_0^c}{\partial t}(y,t); \quad \frac{\partial^2 T_0^d}{\partial y^2}(y,t) = \frac{1}{k^d}\frac{\partial T_0^d}{\partial t}(y,t) \tag{11}$$

$$\frac{\partial^2 T_1^c}{\partial y^2}(y,t) - m^2 T_1^c(y,t) = \frac{1}{k^c}\frac{\partial T_1^c}{\partial t}(y,t);$$

$$\frac{\partial^2 T_1^d}{\partial y^2}(y,t) - m^2 T_1^d(y,t) = \frac{1}{k^d}\frac{\partial T_1^d}{\partial t}(y,t) \tag{12}$$

Since the perturbation is small, we can expand the temperature field in the vicinity of the mean solid/melt interface position, $y = s_0(t)$, in the form of a Taylor series, in which case boundary condition (3) can be written as

$$T_0^c(s_0,t) + \frac{\partial T_0^c(s_0,t)}{\partial y}s_1(t)\cos(mx) + \frac{\partial^2 T_0^c(s_0,t)}{\partial y^2}\frac{s_1^2\cos^2(mx)}{2!} + \left[T_1^c(s_0,t) + \frac{\partial T_1^c(s_0,t)}{\partial y}s_1(t)\cos(mx) + \cdots\right]\cos(mx) = T_m \tag{13}$$

Separating periodic and uniform terms and dropping second and higher order and product terms in the small quantities, T_1 and s_1, we obtain the two first-order equations:

$$T_0^c(s_0,t) = T_m \tag{14}$$

$$s_1(t)\frac{\partial T_0^c}{\partial y}(s_0,t) + T_1^c(s_0,t) = 0 \tag{15}$$

A similar procedure applied to the boundary condition (4) also yields the two equations

$$L^c\rho^c\frac{ds_0(t)}{dt} = K^c\frac{\partial T_0^c}{\partial y}(s_0,t) \tag{16}$$

$$L^c\rho^c\frac{ds_1(t)}{dt} = K^c\left[\frac{\partial T_1^c(s_0,t)}{\partial y} + s_1(t)\frac{\partial^2 T_0^c(s_0,t)}{\partial y^2}\right] \tag{17}$$

The solid/mold boundary condition (5) and (6) give

$$K^c\frac{\partial T_0^c}{\partial y}(0,t) = K^d\frac{\partial T_0^d}{\partial y}(0,t) \tag{18}$$

$$K^c\left\{\frac{\partial^2 T_0^c}{\partial y^2}(0,t)l\epsilon_1 + \frac{\partial T_1^c}{\partial y}(0,t)\right\} = K^d\left\{\frac{\partial^2 T_0^d}{\partial y^2}(0,t)l\epsilon_1 + \frac{\partial T_1^d}{\partial y}(0,t)\right\} \tag{19}$$

$$R_0K^c\frac{\partial T_0^c}{\partial y}(0,t) = T_0^c(0,t) - T_0^d(0,t) \tag{20}$$

$$R_0K^c\left\{\frac{\partial^2 T_0^c}{\partial y^2}(0,t)l\epsilon_1 + \frac{\partial T_1^c}{\partial y}(0,t)\right\} = \left\{\frac{\partial T_0^c}{\partial y}(0,t)l\epsilon_1 + T_1^c(0,t) - \frac{\partial T_0^d}{\partial y}(0,t)l\epsilon_1 - T_1^d(0,t)\right\} \tag{21}$$

Finally, the boundary condition (7) at the bottom of the mold gives the two equations

$$K^d\frac{\partial T_0^d}{\partial y}(-h_0,t) = Q \tag{22}$$

$$\frac{\partial T_1^d}{\partial y}(-h_0,t) = \frac{\partial^2 T_0^d}{\partial y^2}(-h_0,t)l\epsilon_2 \tag{23}$$

Notice that the zeroth-order boundary conditions are identical to that for the unperturbed problem, whereas that for the first-order includes terms derived from the zeroth-order solution. This is typical of the procedure and permits the two problems to be solved sequentially.

It should be noted that Li and Barber [17] developed a linear perturbation model of a planar mold surface based on perturbation of the classical Neumann solution. Their model, however, did not account for the mold properties, and therefore they determined the temperature distribution only in the solid shell. It is therefore not possible to draw any conclusions from their work about the effects of mold properties on the shell thickness non-uniformity and how the mold surface topography wavelength affects the growth instability.

4. Dimensionless presentation

Before proceeding to the solution, it is convenient to introduce the following dimensionless variables

$$Y = my;\quad S_0(\beta) = ms_0(t);\quad S_1(\beta) = \frac{ms_1(t)}{\epsilon_1};\quad H_0 = mh_0;$$
$$\beta = m^2\frac{K^cT_m}{\rho^cL^c}t;\quad \overline{T}_0(Y,\beta) = \frac{T_0(y,t)}{T_m};\quad \overline{T}_1(Y,\beta) = \frac{T_1(y,t)}{\epsilon_1T_m};$$
$$\overline{Q} = \frac{Q}{mK^cT_m};\ R = mK^cR_0;\quad \zeta = \frac{K^c}{K^d};\quad \alpha = \frac{\epsilon_2}{\epsilon_1};$$
$$\Lambda_c = \frac{K^cT_m}{k^c\rho^cL^c};\quad \Lambda_d = \frac{K^cT_m}{k^d\rho^cL^c} \tag{24}$$

The governing equations (10) and (11) for $\overline{T}_0^c(Y,\beta)$, $\overline{T}_0^d(Y,\beta)$ and $\overline{T}_1^c(Y,\beta)$, $\overline{T}_1^d(Y,\beta)$ then become

$$\frac{\partial^2\overline{T}_0^c(Y,\beta)}{\partial Y^2} = \Lambda_c\frac{\partial\overline{T}_0^c(Y,\beta)}{\partial\beta};\quad \frac{\partial^2\overline{T}_0^d(Y,\beta)}{\partial Y^2} = \Lambda_d\frac{\partial\overline{T}_0^d(Y,\beta)}{\partial\beta}; \tag{25}$$

$$\frac{\partial^2\overline{T}_1^c(Y,\beta)}{\partial Y^2} - \overline{T}_1^c(Y,\beta) = \Lambda_c\frac{\partial\overline{T}_1^c(Y,\beta)}{\partial\beta};$$
$$\frac{\partial^2\overline{T}_1^d(Y,\beta)}{\partial Y^2} - \overline{T}_1^d(Y,\beta) = \Lambda_d\frac{\partial\overline{T}_1^d(Y,\beta)}{\partial\beta} \tag{26}$$

The boundary conditions (14), (16), (18), (20), (22), corresponding to the zeroth-order temperature fields $\overline{T}_0^c(Y,\beta)$ and $\overline{T}_0^d(Y,\beta)$, become

$$\overline{T}_0^c(S_0,\beta) = 1 \tag{27}$$

$$\frac{dS_0(\beta)}{d\beta} = \frac{\partial\overline{T}_0^c(S_0,\beta)}{\partial Y} \tag{28}$$

$$R\frac{\partial\overline{T}_0^c(0,\beta)}{\partial Y} = \overline{T}_0^c(0,\beta) - \overline{T}_0^d(0,\beta) \tag{29}$$

$$R\frac{\partial\overline{T}_0^d(0,\beta)}{\partial Y} = \zeta\{\overline{T}_0^c(0,\beta) - \overline{T}_0^d(0,\beta)\} \tag{30}$$

$$\frac{\partial\overline{T}_0^d(-H_0,\beta)}{\partial Y} = \zeta\overline{Q} \tag{31}$$

and the boundary conditions (15), (17), (19), (21), (23), corresponding to the first-order temperature fields $\overline{T}_1^c(Y,\beta)$ and $\overline{T}_1^d(Y,\beta)$, can be written as

$$S_1(\beta)\frac{\partial\overline{T}_0^c(S_0,\beta)}{\partial Y} + \overline{T}_1^c(S_0,\beta) = 0 \tag{32}$$

$$\frac{dS_1(\beta)}{d\beta} = \frac{\partial\overline{T}_1^c(S_0,\beta)}{\partial Y} + S_1(\beta)\frac{\partial^2\overline{T}_0^c(S_0,\beta)}{\partial Y^2} \tag{33}$$

$$\frac{\partial^2\overline{T}_0^c(0,\beta)}{\partial Y^2} + \frac{\partial\overline{T}_1^c(0,\beta)}{\partial Y} = \frac{1}{R}\left\{\frac{\overline{T}_0^c(0,\beta)}{\partial Y} + \overline{T}_1^c(0,\beta) - \frac{\overline{T}_0^d(0,\beta)}{\partial Y} - \overline{T}_1^d(0,\beta)\right\} \tag{34}$$

$$\frac{\partial^2\overline{T}_0^d(0,\beta)}{\partial Y^2} + \frac{\partial\overline{T}_1^d(0,\beta)}{\partial Y} = \frac{\zeta}{R}\left\{\frac{\overline{T}_0^c(0,\beta)}{\partial Y} + \overline{T}_1^c(0,\beta) - \frac{\overline{T}_0^d(0,\beta)}{\partial Y} - \overline{T}_1^d(0,\beta)\right\} \tag{35}$$

$$\frac{\partial\overline{T}_1^d(-H_0,\beta)}{\partial Y} = \alpha\frac{\partial^2\overline{T}_0^d(-H_0,\beta)}{\partial Y^2} \tag{36}$$

Thus, the problem is reduced to the determination of three pairs of functions $\overline{T}_0^c(Y,\beta)$, $\overline{T}_0^d(Y,\beta)$, $S_0(\beta)$ and $\overline{T}_1^c(Y,\beta)$, $\overline{T}_1^d(Y,\beta)$, $S_1(\beta)$ in Eqs. (25) and (26), which satisfy the boundary conditions (27)–(36), respectively.

5. Preview of the algorithm

Eqs. (25) and (26) with boundary conditions in (27)–(36) cannot be solved in closed form, and therefore we must resort to a numerical solution. There are two main approaches to the solution of the problem. One is the front tracking method, where the position of the moving solid–liquid interface is continuously tracked. In this case, the moving phase boundary requires special treatment, and discontinuities tend to arise during time increments for which this boundary passes through one of the grid points. An alternative approach is to use a Lagrangian method where variable space grid and variable time step are used.

In the present work, an explicit finite difference Lagrangian scheme has been implemented. In this case, the zeroth-order solid phase $0 < Y < S_0(t)$, is divided into a fixed number of elements N, so the space step size, $\delta = S_0/N$, increases with time due to the growth in $S_0(t)$. This permits the last node to be identified with the zeroth-order solid–liquid moving front at all times, but implies that the node locations move in time, necessitating the inclusion of convective terms in the updating algorithm for temperature. Thus, for example, the instantaneous zeroth-order solidified layer temperature field is represented by the temperatures at the $N+1$ points $Y=(i-1)\delta$, $i=1,2,\ldots,N+1$. The increase of the shell thickness S_0 during the next time increment τ is determined from the finite difference formulation of Eq. (28):

$$S_0^{j+1} = S_0^j + \frac{\tau}{2\delta}(3\overline{T}^j_{0_{N+1}} - 4\overline{T}^j_{0_N} + \overline{T}^j_{0_{N-1}}) \tag{37}$$

after which the solidified layer temperatures at the interior nodes $i=2,3,\ldots,N$ are updated using the finite difference form of the heat conduction equation (25a):

$$\overline{T}^{j+1}_{0_i} = \overline{T}^j_{0_i} + \frac{\tau}{\Lambda_c\delta^2}(\overline{T}^j_{0_{i+1}} - 2\overline{T}^j_{0_i} + \overline{T}^j_{0_{i-1}}); \quad i=2,3,\ldots,N \tag{38}$$

which can be corrected using convective terms through

$$\overline{T}^{j+1}_{0_i} = \overline{T}^{j+1}_{0_i} + (i-1)\frac{\delta^{j+1}-\delta^j}{\delta^j}\left(\overline{T}^{j+1}_{0_{i+1}} - \overline{T}^{j+1}_{0_i}\right); \quad i=2,3,\ldots,N \tag{39}$$

The solidified layer temperatures at node $N+1$ remain at a constant value for all times in view of Eq. (27) and that at node 1 is updated through (29), which determines the first difference in the first element. Essentially, the same procedure is used to determine the evolution of the first-order solidified layer temperature field, using Eqs. (32)–(36).

The choice of an appropriate value for τ is motivated by the desire for computational efficiency, while retaining acceptable numerical convergence and stability. Extensive investigations were made into the effect of both space and time discretization to ensure that the final results are reliable. With the explicit scheme used here, the maximum time step for stability is proportional to $\Lambda_c\delta^2$ and hence the stability requirement generally places a restriction on τ when good spatial accuracy is desired, necessitating very small values of δ. When the thermal capacities of the shell and mold materials are both considered in the model numerical stability of the scheme is satisfied if

$$\frac{\tau}{\Lambda_c\delta^2} < 0.5; \quad \frac{\tau}{\Lambda_d\delta_d^2} < 0.5 \tag{40}$$

where δ_d and Λ_d are the space step size in the mold and the dimensionless thermal capacity of the mold material, respectively. At the beginning of the process, the solidified shell thickness and δ are very small, and therefore we need an extremely small time step that causes the numerical process to be very slow. However, S_0 and hence δ increases during the process, permitting the time step to be increased as the system evolves without loss of stability if the second condition given in Eq. (40) can be removed. Otherwise, the second condition in Eq. (40) places a very severe restriction on the time increment, τ since δ_d remains constant during the process. Therefore, in the present study, extremely small initial value of δ is required to be used throughout the whole process.

With the algorithm described above, it is clearly not possible to start at the instant of first solidification, since at $S_0 = 0$, all the nodes would coincide. Instead, we need to use an asymptotic solution of the problem at small times to provide a suitable initial condition for the numerical algorithm at finite time. Fortunately, the limiting solution given in the next section, which assumes that diffusivities of the solidified shell and mold materials are both infinitely large, becomes progressively more accurate at small times, since the temperature drop across the solidified layer is small at the very beginning of the process. We can therefore start the process with a small but finite thickness, using the limiting solution given in the following section to define the initial values for the temperature fields in the solidified shell and the mold.

6. Limiting solution

It can be demonstrated that the solution for $\Lambda_c \to 0$ and $\Lambda_d \to 0$ is a limiting case of the present more general theory. This simplification permits the solution to be obtained in closed form and makes possible all the calculations to be performed analytically. The results of limiting case are useful in the development and checking of purely numerical solution of general case, as well as in providing a start-up solution for the general problem.

In physical terms, this simplifying assumption is equivalent to the statement that the casting and the mold materials have zero thermal capacity. In other words, the heat diffusivities of the casting and the mold materials are infinitely large. It then follows that Eq. (25) approximate Laplace's equations and in view of the condition, $\partial s/\partial x \ll 1$, that the temperature profiles in the solidified layer and in the mold are linear in y. In this case Eq. (25) can easily be solved using the boundary conditions (27)–(31) with the result

$$\overline{T}_0^{c}(Y,\beta) = 1 + \overline{Q}[Y - S_0] \tag{41}$$

$$\overline{T}_0^{d}(Y,\beta) = 1 + \overline{Q}[\zeta Y - S_0 - R] \tag{42}$$

Substituting Eq. (41) into (28) and solving the ordinary differential equation for $S_0(\beta)$ we obtain the amplitude of the unperturbed solidification front as

$$S_0(\beta) = \overline{Q}\beta \tag{43}$$

The governing equation for the first-order temperature field in the solid phase and in the mold can be solved remaining boundary conditions (32)–(36) with the result

$$\overline{T}_1^{c}(Y,\beta) = C_1(\beta)\sinh(Y) + C_2(\beta)\cosh(Y) \tag{44}$$

$$\overline{T}_1^{d}(Y,\beta) = C_3(\beta)\sinh(Y) + C_4(\beta)\cosh(Y) \tag{45}$$

where

$$C_1(\beta) = \frac{1}{\Delta}\{(1-\zeta)\cosh(S_0)\sinh(H_0) - S_1\sinh(H_0)\} \tag{46}$$

$$C_2(\beta) = -\frac{1}{\Delta}\{S_1\{\zeta\cosh(H_0) + R\sinh(H_0)\} + (1-\zeta)\sinh(S_0)\sinh(H_0)\} \tag{47}$$

$$C_3(\beta) = \zeta C_1(\beta) \tag{48}$$

$$C_4(\beta) = 1 - \zeta + C_2(\beta) - RC_1(\beta) \tag{49}$$

where

$$\Delta = \sinh(S_0)\sinh(H_0) + \cosh(S_0)\{\zeta\cosh(H_0) + R\sinh(H_0)\} \tag{50}$$

Finally, using Eqs. (33), (41) and (44) we can obtain a differential equation

$$\frac{dS_1(\beta)}{d\beta} = C_1(\beta)\cosh(S_0) + C_2(\beta)\sinh(S_0) \tag{51}$$

for the amplitude of the perturbation in solidification front, with solution

$$S_1(\beta) = \frac{(1-\zeta)\sinh(H_0)S_0 + \zeta\cosh(H_0) + R\sinh(H_0)}{\sinh(S_0)\sinh(H_0) + \cosh(S_0)\{\zeta\cosh(H_0) + R\sinh(H_0)\}} \tag{52}$$

Notice that when H_0 goes to zero in the above equation this limiting solution approaches

$$S_1(\beta) = \frac{1}{\cosh(S_0)} \tag{53}$$

which is equal to the limiting solution for zero Stefan number given in Ref. [18] where the sinusoidal mold of zero thickness is assumed to be thermally rigid.

7. Results and discussion

We wish to examine the variation of the perturbation in solidification front $s_1(t)$ with mean shell thickness $s_1(t)$ for systems where the mold and shell materials are combinations of pure aluminum, iron, and copper. The material properties used in the calculations are listed in Table 1. The symbols T_m, K, ρ, L, and k denote the melting temperature, thermal conductivity, density, latent heat, and thermal diffusivity, respectively. Although it is assumed that each property is a temperature-independent constant, most of the reported values were measured close to the melting temperature of each material.

Table 1
Material properties for pure aluminum and iron at the melting temperature

Property	Material		
	Al	Fe	Cu
T_m (°C)	660	1536	1084
K (W/m °C)	229.4	36.2	345.4
ρ (kg/m^3)	2650	7265	7938
L (10^5J/kg)	3.9	2.7	2.0
ν	0.33	0.33	0.37
k (10^{-5}m^2/s)	8.2	1.61	10.2

The process parameters are chosen to be $R_0 = 10^{-5}$ m^2 s °C/J, $h_0 = 50$ mm, $a_1 = 1.0$ μm, and $\alpha = 0$ (unless otherwise specified).

The numerical algorithm has first been verified by comparing the computed results with the analytical limting solution for the problem with zero heat capacities of the casting and the mold materials. Notice that the parameters Λ_c and Λ_d can be considered as describing the effect of finite thermal diffusivities, or equivalently, of the thermal capacities of the casting and mold materials respectively. The two sets of curves correspond to $\zeta = 0.1$ and 1. There are two curves for each value of ζ: one corresponds to the idealized case of zero heat capacities, $\Lambda_c = \Lambda_d = 0$ which is obtained through analytical calculations (i.e., Eq. (52)), and the other curve is for very small but non-zero thermal capacities of shell and mold materials. Agreement between the analytical and numerical solutions for small heat capacities are seen to be excellent at all times as shown in Fig. 2.

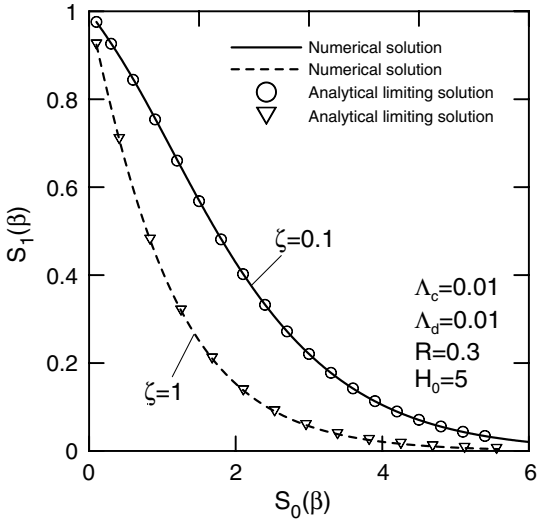

Fig. 2. Numerical and analytical limiting solutions for perturbed solidification front as a function of $S_0(\beta)$ for $R = 0.3$, $H_0 = 5$, $\Lambda_c = 0.01$, $\Lambda_d = 0.01$ for the case where $\xi = 1$ (dashed line), $\xi = 0.1$ (solid line).

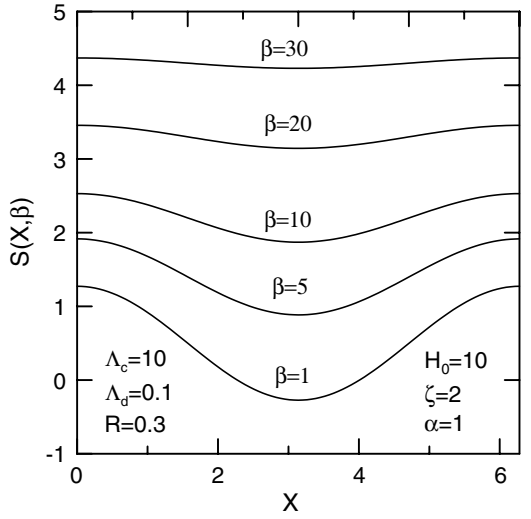

Fig. 3. Growth of the solidified shell with X at various values of the dimensionless time, β, for the case where $\Lambda_c = 10$, $\Lambda_c = 0.1$, $H_0 = 10$, $R = 0.3$, $\alpha = 1$, and $\xi = 2$.

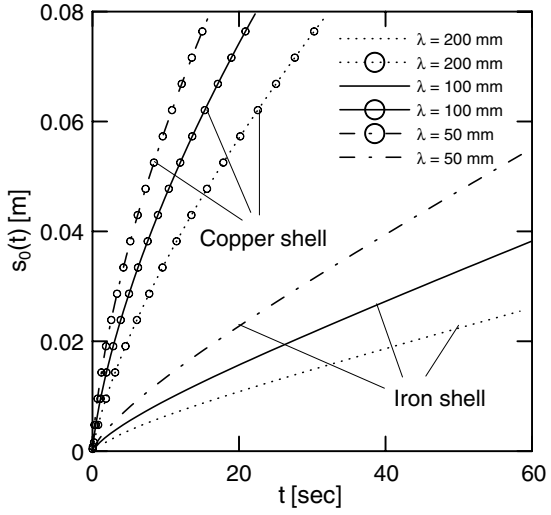

Fig. 5. Evolution of zeroth-order solidification front as a function of time at selected λ for pure copper and pure iron shells solidifying on a pure aluminum mold with $R_0 = 10^{-5}$ m^2 s °C/J, $h_0 = 50$ mm, $\alpha = 0$, $a_1 = 1$ μm.

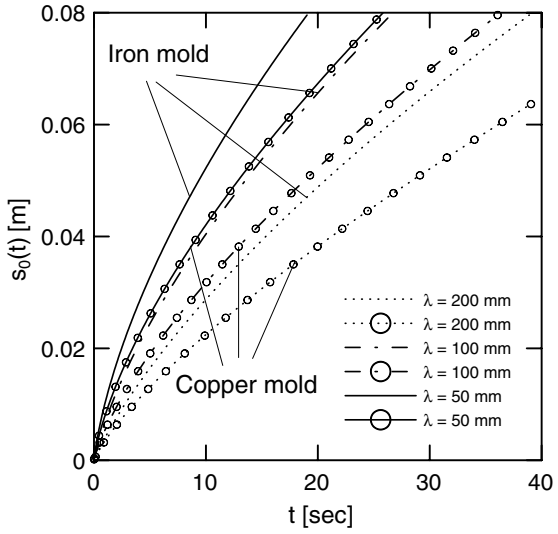

Fig. 4. Evolution of zeroth-order solidification front as a function of time at selected λ for pure aluminum solidifying on pure iron and pure copper molds with $R_0 = 10^{-5}$ m^2 s °C/J, $h_0 = 50$ mm, $\alpha = 0$, $a_1 = 1$ μm.

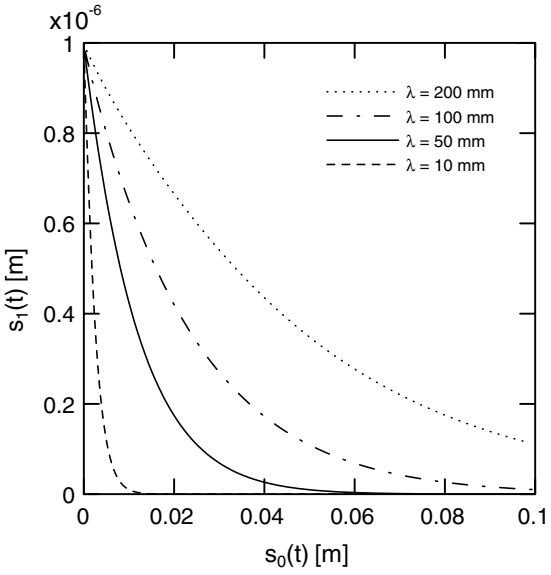

Fig. 6. Evolution of first-order solidification front as a function of mean shell thickness at selected λ for pure aluminum shell solidifying on a pure copper mold with $R_0 = 10^{-5}$ m^2 s °C/J, $h_0 = 50$ mm, $\alpha = 0$, $a_1 = 1$ μm.

Fig. 3 shows the position of the solid-melt interface at various values of the dimensionless time, β. As the solidification proceeds the shell thickness non-uniformity decreases. If solidification is interrupted, periodic thickness non-uniformities at the freezing front will be observed. If solidification is allowed to proceed, however, the non-uniformities tend to die out as the freezing front morphology becomes less dependent upon the mold–shell interface due to the ever-thickening shell. It should be noted that this theoretical result is supported by many experimental observations of thermo-mechanical growth instability in casting processes [5–8].

Figs. 4 and 5 show the growth of mean shell thickness in time for aluminum–iron and aluminum–copper, and copper–aluminum and iron–aluminum shell–mold systems, respectively. Note that $K_{Fe} < K_{Al} < K_{Cu}$. Mold with higher thermal conductivity causes slower growth of mean shell thickness as seen in Fig. 4 whereas shell with higher thermal conductivity causes faster growth of mean shell thickness as seen in Fig. 5. In both cases, the smaller wavelengths lead to faster growth of the mean shell thickness.

Figs. 6 and 7 show the variation of the perturbation in solidification front $s_1(t)$ with mean shell thickness $s_0(t)$ for an aluminum and iron shells solidifying on a copper mold, respectively. Four curves, corresponding to wavelengths of 10 mm, 50 mm, 100 mm, and 200 mm are shown. Fig. 8

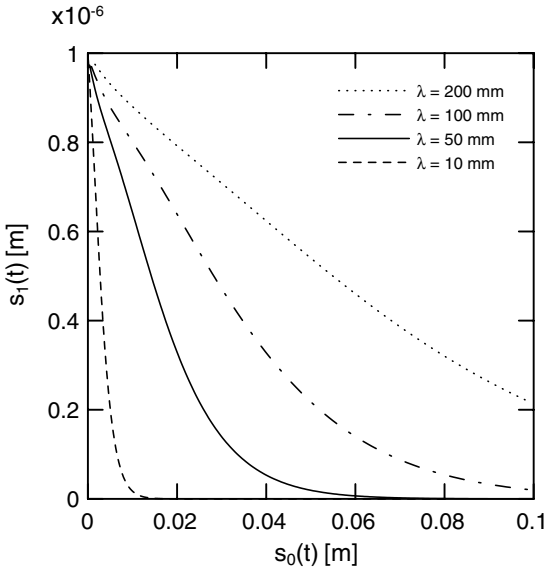

Fig. 7. Evolution of first-order solidification front as a function of mean shell thickness at selected λ for pure iron shell solidifying on a pure copper mold with $R_0 = 10^{-5}$ m^2 s °C/J, $h_0 = 50$ mm, $\alpha = 0$, $a_1 = 1$ μm.

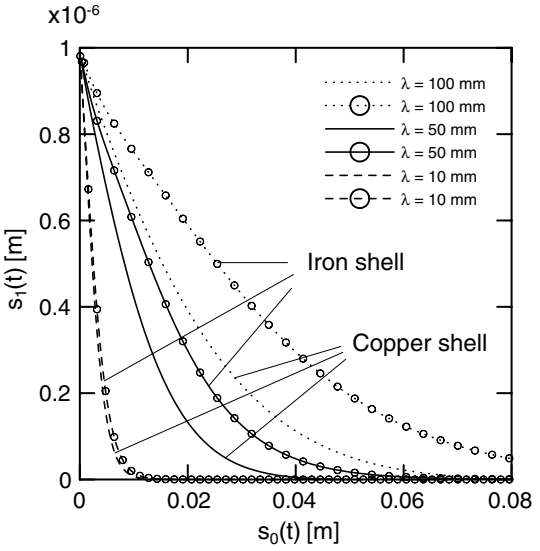

Fig. 9. Variation of first-order solidification front as a function of mean shell thickness at selected λ for pure iron and copper shells solidifying on a pure aluminum mold with $R_0 = 10^{-5}$ m^2 s °C/J, $h_0 = 50$ mm, $\alpha = 0$, $a_1 = 1$ μm.

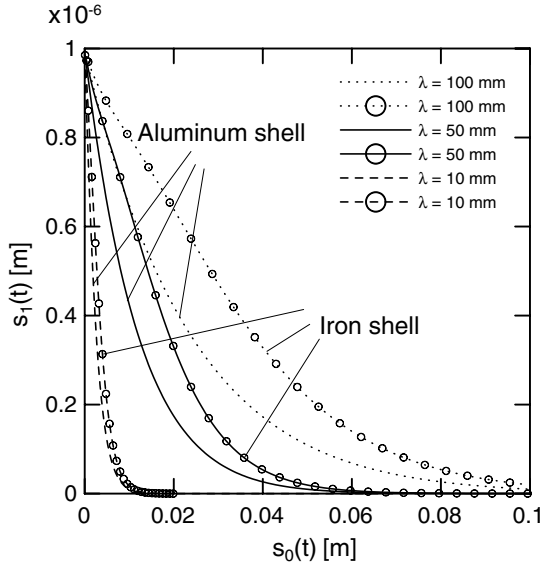

Fig. 8. Variation of first-order solidification front as a function of mean shell thickness at selected λ for pure aluminum and iron shells solidifying on a pure copper mold with $R_0 = 10^{-5}$ m^2 s °C/J, $h_0 = 50$ mm, $\alpha = 0$, $a_1 = 1$ μm.

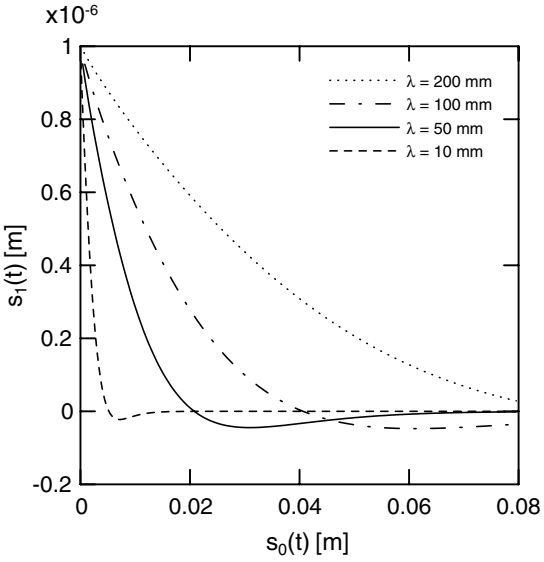

Fig. 10. Variation of first-order solidification front as a function of mean shell thickness at selected λ for pure aluminum shell solidifying on a pure iron mold with $R_0 = 10^{-5}$ m^2 s °C/J, $h_0 = 50$ mm, $\alpha = 0$, $a_1 = 1$ μm.

combines the $s_1(t)$ curves separately considered in Figs. 6 and 7. The ordering of the two curves for each wavelength in Fig. 8 is dictated by the shell thermal capacity. Perturbation in solidification front $s_1(t)$ approaches zero for pure aluminum shell faster than that of pure iron shell since thermal capacity of aluminum is higher than that of iron. This indicates that shell materials with higher thermal capacities (or lower thermal diffusivities) might be less susceptible to growth instability reported in casting experiments [5–8]. Fig. 9 examines the variation of the perturbation in solidification front $s_1(t)$ with mean shell thickness $s_0(t)$ for iron–aluminum and copper–aluminum shell–mold systems. Again, shell with higher thermal capacity causes faster decay of $s_1(t)$ for all λ values considered. It shows that the perturbation in solidification front $s_1(t)$ diminishes at an earlier time and thinner mean shell thickness implying that the shell freezing front is likely to exhibit a planar growth.

Fig. 10 shows the variation of the perturbation in solidification front $s_1(t)$ with mean shell thickness $s_0(t)$ for an

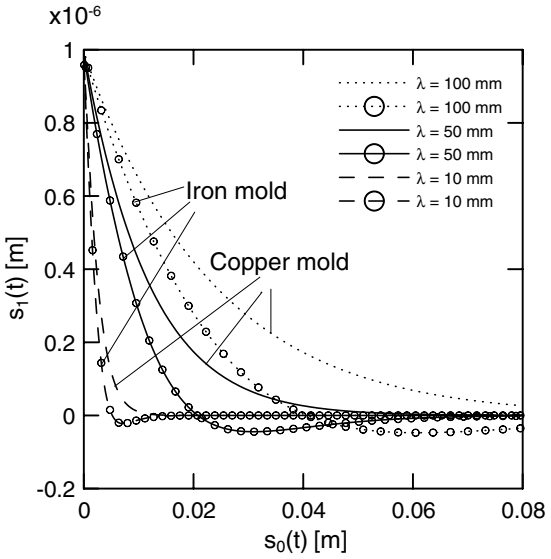

Fig. 11. Variation of first-order solidification front as a function of mean shell thickness at selected λ for pure aluminum shell solidifying on a pure iron and copper molds with $R_0 = 10^{-5}$ m^2 s °C/J, $h_0 = 50$ mm, $\alpha = 0$, $a_1 = 1$ μm.

aluminum shell solidifying on an iron mold. The effect of wavelength is similar to the one reported in previous cases except that a little overshoot becomes evident as the wavelengths are decreased. This is probably because of the shell–mold material thermal capacity ratio, Λ_c/Λ_d, effect on the growth instability. In Figs. 6 and 7, Λ_c/Λ_d was 0.77 and 0.75, respectively (i.e., less than unity). However, in Fig. 10, $\Lambda_c/\Lambda_d = 1.02$ which is larger than unity. In other words, heat storage capacity of the shell is more than that of mold, which might be the reason of overshoot in $s_1(t)$. To examine the effect of mold material thermal capacity on the growth instability, Fig. 11 is reported. This figure combines the $s_1(t)$ curves separately considered in Figs. 4 and 10 where the shell material is kept constant as a pure aluminum for both cases. Iron mold causes faster decay than copper mold for each wavelength considered. This indicates that mold materials with higher thermal capacities might be less prone to growth instability in solidification.

Current work on this problem is focused on a fully coupled version of the present problem that includes the effect of mechanical problems (i.e., stress fields in the solidified shell thickness and the mold, and contact pressure variations in the shell–mold interface). This requires that the thermoelastic stress fields in the solidified shell thickness and the mold to be added into the thermal fields presented in this work. The present theory does not account for this important phenomenon and, hence, predictions made about the growth instability here are clearly very restrictive. It is anticipated that the fully coupled version of the present problem may provide conclusive demonstration of the proposed growth instability mechanism observed in many casting experiments.

8. Conclusions

The heat conduction problem has been investigated in which one dimensional solidification process occurs on a sinusoidal mold of low aspect ratio (i.e., the ratio of the amplitude to wavelength is much less than one). In particular, numerical solutions have been obtained for the advance of the solid/melt boundary. The effect of thermal diffusivities of the solidified shell and the mold materials was also investigated. It was demonstrated that the solidified shell material with higher thermal capacity might result in planar shell growth, whereas the mold material with higher thermal conductivity may cause irregular growth of the shell which, generally, causes cracking near the surface. We have also briefly discussed the limiting solution for $\Lambda_c = \Lambda_d = 0$, in which the zeroth-order temperature profiles in the solid and in the mold are linear in y. This simplification permits the problem to be solved analytically.

The results of the present analysis can be used in determining the residual thermoelastic stresses in solidification of pure metals on a sinusoidal and deformable mold surface. This problem is the subject of an ongoing investigation and will be reported elsewhere.

References

[1] H.S. Carslaw, J.C. Jaeger, Conduction of Heat in Solids, 2nd ed., Oxford University Press, London, England, 1956, pp. 282–296.
[2] N.-Y. Li, Thermomechanical stresses and some asymptotic behavior in casting with spherical solidification, J. Thermal Stresses 18 (1995) 165–184.
[3] M.N. Ozisik, Heat Conduction, Wiley, New York, 1980, pp. 397–438.
[4] M.N. Ozisik, S.I. Guceri, A variable eigenvalue approach to the solution of phase-change problems, Can. J. Chem. Engng. 55 (1977) 145–148.
[5] Y. Sugitani, M. Nakamura, M. Okuda, M. Kawasaki, S. Miyahara, Control of uneven solidified shell formation of hypo-peritectic carbon steels in continuous casting mold, Trans. Iron Steel Inst. Japan 25 (1992) B–91.
[6] J. Cisse, G. Cole, G. Bolling, Freezing front asymmetry during ingot solidification of aluminum and its alloys, AFS Cast Met. Res. J. 7 (1971) 158–161.
[7] S. Singh, K. Blazek, Heat transfer and skin formation in a continuous casting mold as a function of steel carbon content, J. Met. (1974) 17–27.
[8] P.J. Wray, Geometric features of chill-cast surfaces, Met. Trans. B 12B (1981) 167–176.
[9] O. Richmond, L.G. Hector Jr., J.M. Fridy, Growth instability during non-uniform directional solidification of pure metals, ASME J. Appl. Mech. 57 (1990) 529–536.
[10] F. Yigit, N.-Y. Li, J.R. Barber, Effect of thermal capacity on thermoelastic instability during the solidification of pure metals, J. Thermal Stresses 16 (1993) 285–309.
[11] F. Yigit, J.R. Barber, Effect of Stefan number on thermoelastic instabilities in unidirectional solidification, Int. J. Mech. Sci. 36 (8) (1994) 707–723.
[12] F. Yigit, L.G. Hector Jr., Critical wavelengths for gap nucleation in solidification. part 1: theoretical methodology, ASME J. Appl. Mech. 67 (2000) 66–76.
[13] F. Yigit, L.G. Hector Jr., Critical wavelengths for gap nucleation in solidification. Part 2. Results for selected mold–shell material combinations, ASME J. Appl. Mech. 67 (2000) 77–86.

[14] K. Buxmann, M. Boliger, I. Gyongyos, Mould with Roughened Surface for Casting Metals, US Letters Patent #4,250,950, 1981.
[15] H. Murakami, M. Suzuki, T. Kitagawa, S. Miyahara, Control of uneven solidified shell formation of hypo-peritectic carbon steels in continuous casting mold, J. Iron Steel Inst. Jpn. 78 (1992) 105–112.
[16] D.A. Weirauch Jr., A. Giron, The early stages of aluminum solidification in the presence of a moving meniscus, in: Proceedings on the Integration of Material Process and Product Design – A Conference Dedicated to the 70th birthday of Owen Richmond, A.A. Balkema Publishers, Rotterdam, Netherlands, 1998, pp. 183–191.
[17] N.-Y. Li, J.R. Barber, Sinusoidal perturbation solutions for planar solidification, Int. J. Heat Mass Transfer 32 (1989) 935–941.
[18] L.G. Hector Jr., J.A. Howarth, O. Richmond, W.-S. Kim, Mold surface wavelength effect on gap nucleation in solidification, ASME J. Appl. Mech. 67 (1999) 155–164.